**The NanoSIMS-HR: the next generation of high spatial resolution dynamic SIMS**

Peter K. Weber* - Physical and Life Sciences, Lawrence Livermore National Laboratory, Livermore, CA 94505, USA. email: weber21@llnl.gov

Marc Debliqui - CAMECA Instruments, 29 quai des Grésillons, 92622 Gennevilliers, France.

Céline Defouilloy - CAMECA Instruments, 29 quai des Grésillons, 92622 Gennevilliers, France.

Xavier Mayali - Physical and Life Sciences, Lawrence Livermore National Laboratory, Livermore, CA 94505, USA.

Ming-Chang Liu - Physical and Life Sciences, Lawrence Livermore National Laboratory, Livermore, CA 94505, USA.

Rachel Hestrin - University of Massachusetts, Amherst, 161 Holdsworth Way, Amherst, MA 01003, USA.

Jennifer Pett-Ridge - Physical and Life Sciences, Lawrence Livermore National Laboratory, Livermore, CA 94505, USA and Life & Environmental Sciences Department, University of California Merced, 5200 North Lake Rd., Merced, CA 95343, USA.

Rhona Stuart - Physical and Life Sciences, Lawrence Livermore National Laboratory, Livermore, CA 94505, USA.

Megan Morris[#] - Physical and Life Sciences, Lawrence Livermore National Laboratory, Livermore, CA 94505, USA.

Christina Ramon - Physical and Life Sciences, Lawrence Livermore National Laboratory, Livermore, CA 94505, USA.

Danielle M. Jorgens - Electron Microscope Laboratory, University of California, Berkeley, 21 Barker Hall, Berkeley, CA 94720, USA.

Reena Zalpuri - Electron Microscope Laboratory, University of California, Berkeley, 21 Barker Hall, Berkeley, CA 94720, USA.

Laurent Arnoldi - CAMECA Instruments, 29 quai des Grésillons, 92622 Gennevilliers, France.

Jérôme Farcy - CAMECA Instruments, 29 quai des Grésillons, 92622 Gennevilliers, France.

Nicolas Saquet - CAMECA Instruments, 29 quai des Grésillons, 92622 Gennevilliers, France.

Sarah Vitcher Fichou - CAMECA Instruments, 29 quai des Grésillons, 92622 Gennevilliers, France.

Ludovic Renaud - CAMECA Instruments, 29 quai des Grésillons, 92622 Gennevilliers, France.

Aurélien Thomen - CAMECA Instruments, 29 quai des Grésillons, 92622 Gennevilliers, France.

## Abstract

The high lateral resolution and sensitivity of the NanoSIMS 50 and 50L series of dynamic SIMS instruments has enabled numerous scientific advances over the past 25 years. Here we report on the NanoSIMS-HR, the first major upgrade to the series, and analytical tests in a suite of sample types, including an aluminum sample containing silicon crystals, microalgae and plant roots colonized with arbuscular mycorrhizal fungi. Significant improvements have been made in the $Cs^+$ ion source, high voltage (HV) control, stage reproducibility, and other aspects of the instrument that affect performance. The modified design of the NanoSIMS-HR thermal-ionization $Cs^+$ source enables a 5-pA primary ion beam to be focused into a 100 nm spot, a ~2.5-fold increase compared to $Cs^+$ sources on previous instruments (~2 pA at 100 nm). The brightness of the new $Cs^+$ source enables an ultimate lateral resolution as high as 30 nm and improved detection limits for a given analysis area. Sample stage movement accuracy is higher than 500 nm, enabling many-fold higher throughput automated analyses. With the new HV control, the primary ion beam impact energy can be reduced from 16 keV to 2 keV, which enables higher depth resolution during depth profiling (a 2-fold improvement), albeit with a 5-fold decrease in lateral resolution. In the NanoSIMS-HR, the secondary ion column and detection system are identical to those used in the previous series, and isotopic analysis performance is as precise as in previous NanoSIMS instruments.

## Introduction

Secondary ion mass spectrometry (SIMS) is a spatially resolved analytical method for characterizing solid samples. First invented in the 1960s [1, 2], SIMS instruments have been developed along multiple lines of emphasis, with the class of magnetic sector “dynamic SIMS” instruments emphasizing high-sensitivity elemental and isotopic analyses [3]. In the 1990s, Georges Slodzian, the inventor of SIMS, conceptualized a coaxial design that enabled dynamic SIMS with higher lateral resolution by improving the primary ion beam focusing for scanning ion imaging [4, 5]. Further developed by Francois Hillion and others, that design became the basis for the NanoSIMS 50 series of instruments [6]. The key capabilities of these instruments are high mass resolving power (>9000 M/$\Delta$M) with high transmission (up to 25%) at high-lateral resolution (as good as 50 nm) [7]. Five (NanoSIMS 50) or seven (NanoSIMS 50L) detectors can also be positioned for simultaneous detection to increase the fraction of ions detected from the sampled volume.

The NanoSIMS 50 series capabilities translate to high mass specificity and sensitivity for the analysis of small features and have enabled discoveries in fields as diverse as cosmochemistry, geology, soil science, structural biology, biomedical research, microbial ecology, and material science [8-12]. Inspired by these successes, the scientific and analytical communities have sought improvements to the NanoSIMS 50 series to further improve spatial resolution, analytical performance and throughput.

50 nanometer lateral resolution has been a featured aspect of the NanoSIMS instruments. NanoSIMS instruments use a normal-incidence primary ion beam with a 16 keV impact energy to sputter the sample to generate secondary ions for analysis [6]. At this energy, the primary ion beam can be finely focused for scanning secondary ion imaging. However, to achieve 50 nm lateral resolution, the primary current must be reduced by ~10x over typical operating conditions for biological samples (Mayali et al. 2023) increasing the analysis time proportionally.

Primary ion source intensity ("brightness") is a factor controlling in the relationship between primary ion beam spot size and current [13], and multiple efforts have been made to increase both the positive cesium ion source—used to enhance the yield of negative secondary ions [14, 15], and the negative oxygen ion source—used to enhance the yield of positive secondary ions [13, 16]. Increased ion source brightness would improve the lateral resolution of NanoSIMS instruments, allowing smaller features—from viruses to presolar grains—to be resolved.

Increased source brightness would also allow higher beam current analyses for lower resolution spot sizes, with the benefits of faster analyses, reduced ion counts from gas phase contribution, and fewer detector dark counts, thereby reducing limits of detection [3].

Increased source brightness could also be leveraged to increase the depth resolution of NanoSIMS analyses while maintaining high lateral resolution. Depth profiling—the practice of using the primary ion beam to erode through the sample while collecting compositional data—is a standard SIMS method that can achieve a few nanometer depth resolution [3]. By comparison, the depth resolution of the NanoSIMS series of instruments is on the order of 10s of nanometers because the normal incident 16 keV primary ion beam penetrates into the sample to depths >20 nm [17]. Depth resolution could be improved by lowering the primary ion beam impact energy, but at the cost of lower lateral resolution. Higher source brightness would regain some of the loss in lateral resolution, which would allow depth profiling of features that cannot be resolved with standard SIMS instruments, such as thin film transistors and attached bacteria.

While NanoSIMS data can be quantitated to the extent that standards and good analytical and statistical practices are used, the small scale of the analyses (typically less than 50 x 50 $\mu m^2$) can present challenges with translating the results to the population scale. This issue is often encountered in microbial ecology studies, where single cell incorporation of an isotopically labeled substrate can vary by over 10x among cells [18] and some cell types can be relatively rare, such as non-cyanobacterial nitrogen fixing bacteria in the open ocean [19]. As a result, there is demand for automation and high throughput to increase data set sizes to collect representative samples. Cosmochemistry and other fields have similar needs. As discussed above, a higher brightness primary ion source is one potential route for increasing throughput. Other factors include stage reproducibility and navigation.

Here we test a new NanoSIMS-HR instrument for lateral resolution, depth resolution, limits of detection, stage reproducibility, and isotopic ratio reproducibility. Lateral resolution measurements were conducted on an aluminum sample containing silicon crystals, and representative images were collected for (1) microalgae and (2) plant roots colonized with arbuscular mycorrhizal fungi. Depth resolution measurements were conducted on a delta layer sample at 16, 8, and 4 keV impact energy. Limit of detection measurements were made on a phosphorus implant. Isotopic ratio data were collected on a Si wafer and a quartz standard.

**Experimental Section**

*Instrument:* The NanoSIMS-HR, like its predecessors the NanoSIMS 50 and 50L, is a scanning ion microprobe coupled to a double-focusing mass spectrometer with a Mattauch-Herzog design, which enables multicollection of secondary ions over a large relative mass range (~22x for the 50L) [4-6, 20]. The primary ions are accelerated toward the sample surface and steered and focused to the desired spot size by a suite of Einzel lenses and deflectors. To optimize focusing, the instrument is designed so that the

primary and secondary ions travel in opposite directions through a single "coaxial" lens stack near the sample. As a result, the primary ion source and the sample surface must be at the same potential and opposite polarity. Normal operation is with the source and sample at |8000V|, resulting in a primary ion impact energy of 16 keV. The NanoSIMS-HR multicollection system has seven detectors, six of which are on movable trolleys to enable mass selection. Electron multiplier (EM) ion detectors in pulse counting mode are used to enable imaging; these can be swapped for Faraday cups (FC) for high-current, higher-precision isotope measurements. Relative to its predecessor instruments, the NanoSIMS-HR includes several key upgrades:

Upgraded item 1: The ionizer, extraction optics and reservoir of the thermal $Cs^+$ primary ion source were redesigned to optimize the angular intensity of the $Cs^+$ beam, improving brightness. For operations in positive polarity, the NanoSIMS-HR has the same radio frequency plasma $O^-$ source [21] included with the NanoSIMS 50L; analyses using that source are not included herein.

Upgraded item 2: The HV boards and electronics were redesigned to allow the primary ion source and sample to be changed to enable low-impact energy analyses. The range of operation is from the standard 16 keV impact energy to 2 keV.

Upgraded item 3: The analysis chamber sample stage has been upgraded to include a position encoder from Horiba Scientific. This sample stage enables sample navigation over a 50 x 50 $mm^2$ sample holder, as well as between SIMS analysis, optical imaging and primary ion beam measurement positions, requiring up to 100 mm in movement. To increase point reproducibility, the stage is equipped with an encoded plate used as a coordinate reference. An optical microscope equipped with a camera monitors the encoded plate to determine the absolute coordinates of the sample holder.

In addition, we note here that the NanoSIMS-HR includes navigation upgrades related to the fact that the sample cannot be observed with an optical system while in the SIMS position because the coaxial lens is too close. As a result, to navigate the sample with optical imaging, the sample holder is moved approximately 40 mm to position the sample in front of an optical objective. In the NanoSIMS-HR, the optical system has been improved to allow approximately ≤1-micron lateral resolution light imaging and mosaic image collection co-registered with the ion beam for SIMS-mode navigation.

*Lateral resolution analyses*

To compare lateral resolution of the NanoSIMS-HR to a NanoSIMS 50L, measurements were made on an aluminum sample with high silicon content ("Al-Si sample") because the Si forms Al-free domains that provide sharp chemical contrast for these measurements. The sample was polished with diamond paste down to 0.1 micron (Buehler) and then colloidal silica (Buehler). Additional imaging was performed with biological samples, detailed below.

Lateral resolution was determined for a range of primary $Cs^+$ beam currents (~0.2 pA to 600 pA) and impact energies (16 keV to 2 keV). Primary ion current selection and focusing was performed as is typical for NanoSIMS instruments. Ion currents were controlled using Einzel lenses (L0 and L1) and a primary beam limiting aperture (D1) located in the coaxial optics column, astigmatism was corrected with an octopole, and the final focusing of the primary beam onto the sample surface was performed with E0P, a lens in the coaxial lens stack. The impact energy was adjusted by sweeping the potential of the source tube containing the Cs reservoir and adjusting the sample potential to the optimized value. High voltages

on the lenses and deflectors in between for primary and secondary optics were scaled down with the energy decrease. Imaging was performed with electron multipliers in pulse counting mode and secondary electrons (SE). The mass spectrometer was operated without an entrance or aperture slit (~2000 mass resolving power (MRP)) for the highest lateral resolution (lowest primary beam current) analyses to achieve the most precise beam resolution measurements by optimizing ion transmission. The beam size was measured by imaging an Al-Si sample with $^{28}Si^-$. $^{27}Al^1H^-$ counts at mass 28 were negligible. Image collection parameters were set to provide a beam overlap from 75% for high lateral resolution image to 99% for large beam for NanoSIMS 50L and from 85% to 97n% for NanoSIMS-HR (2 x 2 to 20 x 20 $\mu m^2$ for NanoSIMS-HR and 5 x 5 to 12 x 12 $\mu m^2$ for the NanoSIMS 50L; all with 512 x 512 pixels; beam overlap defined as the [beam diameter - pixel width] ÷ beam diameter x 100% ). The dwell time varied from 0.2 to 3 milliseconds per pixel. As the intensity profile across two chemically contrasting phases (Al and Si in this case) is a convolution between the sharp edge and gaussian beam intensity distribution, a cumulative gaussian distribution model was used to describe the $^{28}Si^-$ profile. Beam size was defined as the distance represented by the 16 to 84% quantile of the intensity distribution containing 68% of the beam intensity. Ion count transects across selected features were extracted in WinImage ion image data processing software (CAMECA) using a region of interest (ROI) of 2 to 4 pixels wide line by 1 pixel deep to average adjacent pixels perpendicular. Lateral resolution was calculated in WinCurve data processing software (CAMECA) using a cumulative Gaussian distribution model to extract 16% and 84% beam intensity locations on the profile abscissa as the beam size or lateral resolution[22].

*Biological sample imaging*

For comparison to the Al-Si measurements, biological samples were imaged with $^{13}C^{12}C^-$ and $^{12}C^{14}N^-$ secondary ions generated by $Cs^+$ primary ions.

The microalga *Phaeodactylum tricornutum* (CCMP2561, Bigelow National Center for Marine Algae and Microbiota) was imaged to illustrate the different analysis conditions. The microalga was grown on $^{13}C$ and $^{15}N$ labeled inorganic C and N for 48 hours, then fixed with 10% formalin overnight and filtered onto 2 µm pore size polycarbonate membranes and rinsed with double distilled water. Filters were dried overnight at 50°C prior to excising a portion to mount onto a conductive carbon tab (Ted Pella, California, U.S.A.) adhered to an aluminum stub. Mounted samples were sputter coated with ~5 nm of gold.

A thin section of a mycorrhizal root sample was imaged for correlation with transmission electron micrographs. The sample was prepared from the grass *Panicum hallii* infected with the arbuscular mycorrhizal fungus *Rhizophagus irregularis* (formerly *Glomus intraradices*), grown as described in Hestrin et al. (2022). *P. hallii* seeds were germinated on Petri plates, transferred into cones filled with double-autoclaved sand, inoculated with ~500 *R. irregularis* spores, and grown for eight weeks before being transplanted into cones filled with a 50:50 (v:v) mixture of double-autoclaved sand and a fine sandy loam soil collected from a pasture in Caddo County, OK (35.072417/−98.303667). The sand:soil mixture began at 15% moisture and declined to 5% over the course of the 3-month greenhouse experiment. The plants were grown with a 16 hr photoperiod and average daytime and nighttime temperatures of 27 °C and 24 °C, respectively. At harvest, roots were washed, fixed in 50% ethanol, and stored at 4 °C. To prepare samples for imaging, 1-2 mm root segments were excised and transferred to a fresh fixative buffer (2% Tween, 3% glutaraldehyde, 3% paraformaldehyde in 0.05M sodium cacodylate buffer, pH 7.2 (EMS, Hatfield, PA, USA)) and microwaved (Pelco BioWave; Ted Pella, Redding, CA, USA) while under vacuum at room temperature (2**×;** 1 min 150 W (watts) – hold 1 min – 1 min 150 W – hold 1 min – 1 min

150 W; 27 mbar (20 mm Hg vacuum)). Samples were then held under vacuum for 1 hr and stored overnight at 4 °C. Sample were rinsed (3×; 10 min) in 0.05M sodium cacodylate buffer (pH 7.2) and then immersed in a solution of 1% osmium tetroxide with 1.6% potassium ferricyanide in 0.05M sodium cacodylate buffer and microwaved (2×; 1 min 150 W – hold 1 min; 27 mbar at room temperature). Samples were rinsed in a solution of 0.05M sodium cacodylate buffer, pH 7.2 (3×; 10 min at room temperature) and then subjected to an ascending acetone gradient (10 min; 35%, 50%, 70%, 80%, 90%, 100%) followed by pure acetone (3×; 10 min at room temperature). Samples were progressively infiltrated while rocking with Epon resin and acetone mixtures (EMS, Hatfield, PA, USA). For the final 3 exchanges of 100% Epon resin, samples were microwaved at room temperature (1×; 1 min 250 W – hold 1 min; 27 mbar) and then rocked for 2 hr at each step. Finally, samples were polymerized at 60 °C for 48 hours. Thin sections were cut using a Leica UC6 (Leica, Wetzlar, Germany). A 90 nm thin section was collected onto a formvar-coated copper-rhodium backed slot grid. The grid was post-stained for TEM imaging with 2% uranyl acetate followed by Reynold's lead citrate, for 5 min each. The section was imaged with a Tecnai 12 120-keV TEM (FEI, Hillsboro, OR, USA). Image data were recorded using a Gatan Rio16 CMOS camera with GWS software (Gatan Inc., Pleasanton, CA, USA). TEM sections were then sputter coated with ~5 nm of gold.

*Depth resolution analyses*

Depth resolution measurements were made using a custom "delta layer" sample consisting of a silicon substrate with thin phosphorus-rich layers of up to 5% P atoms per Si atoms ($2.5 \times 10^{21}$ P at./cm$^3$) laid down by vapor deposition between silicon layers. The P-rich layers were at 30, 90, 180 and 330 nm depth from the surface (ihp-microelectronics.com). Depth profiles were acquired by using a $Cs^+$ primary beam from 16 keV to 4 keV at 500 pA and by rastering a 20 x 20 µm$^2$ area. MRP was >9000 at 8 keV of secondary ions energy as reported by the NanoSIMS software (based on peak side slope width from 10% to 90% of peak height; equivalent to ~6000 MRP for peak width at 10% height) [23-25]. $^{31}P^-$ and $^{30}Si^-$ images were acquired with a counting time per frame of 4 s for a total acquisition time of about an hour. Images were processed with WinImage by defining a ROI of 8 x 8 µm$^2$ in the image center to extract the counts rates of phosphorus with minimal ion contributions from the analysis periphery. Profiles were then processed with WinCurve to scale the depth and extract depth resolution. Because P is known to diffuse into the overlying Si during deposition but not into the deeper layer (verified by IMS-7f), depth resolution was based on the rate at which the $^{31}P^-$ counts drop off after each layer.

*Measurements of P detection limit in Si wafer with $Cs^+$ analysis*

P detection limits were measured using a P-implanted silicon wafer for a range of $Cs^+$ primary currents and raster sizes to determine the minimum detection limit and optimal raster for each primary current setting. The dose of P was $5.48 \times 10^{13}$ at./cm$^3$ implanted at 200 keV. The peak of the implant was at a depth of 250 nm (± 1%), verified by IMS-WF relative to NIST SRM 2133. The NanoSIMS-HR was tuned for >9000 MRP (10%-90% definition) with entrance slit (ES) 4, aperture slit (AS) 3, and a fully open energy slit (EnS) to simultaneously collect $^{31}P^-$ and $^{30}Si^-$. The $Cs^+$ current on the sample was varied from 10 pA to 8000 pA, and the raster size was varied from 2 x 2 µm$^2$ to 40 x 40 µm$^2$ to test the optimal pairing of primary current and raster size. Depth profiles were collected in imaging mode with 128 x 128 to 256 x 256 pixels for 130 to 400 cycles. The data were processed with WinImage to extract depth profiles from ROIs ranging from the full image down to 10% of the imaged area, with the ROI always in the center of the image. Depth profiles were processed with Wincurve. Ion counts were converted to concentration

(in P at./cm$^3$) as a function of depth after deriving a relative sensitivity factor based on the known total dose. The apparent P concentration in the background tail of the P profile, where no P is sputtered and background dominates the signal, is defined as the detection limit.

*Stage performance*

The stage movement reproducibility was measured by moving the stage ~40 mm away from the center location and back and then performing an internal measurement of the shift in subsequent ion images. A standard deviation on shifts in both directions is deemed as an estimation of the reproducibility of the movement. To test this performance, $^{28}Si^-$ ion images were acquired by scanning a 12 x 12 µm$^2$ area defined with 512 x 512 pixels and a dwell time of 0.3 ms/pixel, and a lateral resolution of 120 nm. An image was acquired in ~80 s in SIMS position, then the sample stage was moved in front of the optical microscope and moved back again in SIMS position for a subsequent image acquisition. This sequence was repeated until a total of 8 images were acquired. WinImage was then used to calculate the shift between 2 consecutive images. An algorithm of image registration with a subpixel precision [22] calculated the shifts in x and y directions. The first image was defined as the reference image, and image shifts in both directions were calculated from it.

*Isotopic ratio measurements*

Multicollection (simultaneous) isotope ratio measurements were made with three different configurations: (1) three Si isotopes ($^{28}Si^-$, $^{29}Si^-$ and $^{30}Si^-$) from silicon wafers (conductor) with ~1 pA $Cs^+$ and 4 x 4 µm$^2$ rasters measured on three EMs, (2) three Si isotopes from the same Si wafers with 600 pA $Cs^+$ and 10 x10 µm² rasters measured on three FCs, (3) oxygen isotopes ($^{16}O^-$ and $^{18}O^-$) from a polished Pt-coated quartz substrate (insulator) with 15 nA $Cs^+$ and 10 x10 µm² rasters measured on two FCs. The normal-incidence electron flood gun was used for charge compensation. The NanoSIMS-HR was tuned for >7000 MRP (10%-90% definition). Data were collected in multicollection “isotope mode” with 64 x 64 pixels. The duration of one analysis, including pre-analysis sputtering, automatic secondary ion beam focusing and centering, automatic mass line centering, and data acquisition, was 10 min, 2 min 30 sec, and 3 min, respectively. Multiple reproducibility tests were conducted, including tests with small (microns), medium (millimeters), and large (10s of millimeters) movements (Table S1; see also Results). Magnet stability was maintained with NMR control.

**Results**

*Lateral Resolution*

Lateral resolution as a function of the primary $Cs^+$ ion current with 16 keV impact energy was quantified for the NanoSIMS-HR and a NanoSIMS 50L with the same Al-Si sample (Fig. 1 & S1; Table S2). For the NanoSIMS-HR tests, the primary current on the sample was set to values from $\leq$0.2 pA $Cs^+$ (below Faraday Cup detection limit) to 600 pA $Cs^+$. The best lateral resolution for the NanoSIMS-HR $Cs^+$ source was 25 nm, compared to 45 nm for the 50L. The specifications are set to 30 nm and 50 nm, respectively. The NanoSIMS-HR resolution at 600 pA was ~600 nm, compared to 100 pA for similar resolution with the 50L. At 100 nm lateral resolution, the data show a 2.5-fold improvement in current density for the NanoSIMS-HR over the NanoSIMS 50L.

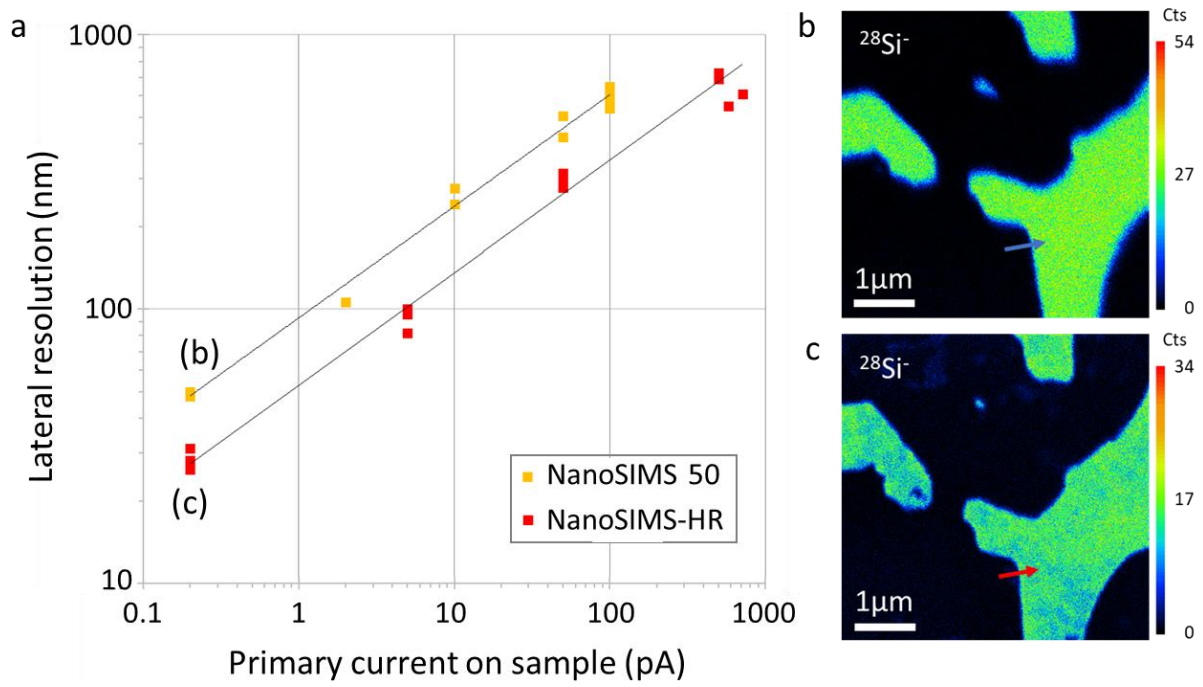


**Figure 1.** (a) Comparison of lateral resolution vs. $Cs^+$ primary current for the NanoSIMS 50L and the NanoSIMS-HR on an Al-Si sample. Correlated Al-Si sample images at the ultimate resolution (≤0.2 pA) for (b) a NanoSIMS 50L with ~45 nm lateral resolution and (c) the NanoSIMS-HR with ~25 nm lateral resolution. Arrows indicate example locations where lateral resolution was measured. The difference in ion counts (cts) per pixel is the result of different dwell times (1200 vs. 800 µs/pixel, respectively); the maximum $^{28}Si^-$ count rates were 43000 and 45000, respectively. See also Fig. S1.

We tested the improved lateral resolution of NanoSIMS-HR on a biological sample by imaging *P. tricornutum* algal cells with the ultimate resolution of the two instruments at 16 keV (Fig. 2). At ~30 nm lateral resolution, the ion images revealed small holes in the algal cell that would not be distinguishable with a standard NanoSIMS 50L, even at the ultimate resolution of 50 nm. These holes form during the sputtering of the *P. tricornutum* cell wall. We also tested the ability of the NanoSIMS-HR to deliver more current within a 100 nm spot. As expected, the secondary ion current increased 2.5x, proportional to the increase in current density.

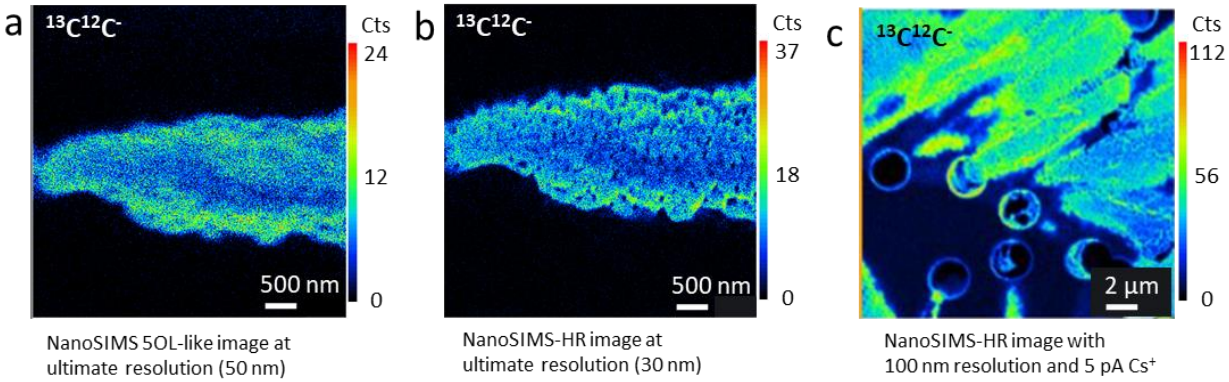


**Figure 2.** $^{13}C^{12}C^-$ ion images of the alga *P. tricornutum* show the difference in ultimate resolution for (a) NanoSIMS 50L and (b) NanoSIMS-HR. At 30 nm lateral resolution, small holes in the *P. tricornutum* cell can be clearly visualized with the NanoSIMS-HR, but not with a standard NanoSIMS 50L. (c) The NanoSIMS-HR can deliver ~2.5x current at 100 nm lateral resolution.

High-lateral-resolution NanoSIMS-HR analyses were also conducted on a 90-nm-thick section of a *P. hallii* root infected with *R. irregularis*, an arbuscular mycorrhizal fungus (Fig. 3 & S2). Figure 3 shows correlated TEM and NanoSIMS-HR $^{12}C^{14}N^-$ images of a subportion of an *R. irregularis* vesicle in the root tissue. The $^{12}C^{14}N^-$ image was collected with the 30 nm lateral resolution settings. The NanoSIMS-HR $^{12}C^{14}N^-$ image shows details that could be seen in the TEM image, as well as chemical contrast that could not. The TEM image shows sub-micron structures inside the vesicle that were visualized with the $^{12}C^{14}N^-$ ion in the NanoSIMS-HR, indicating that it was N-rich. The NanoSIMS-HR $^{12}C^{14}N^-$ image also shows that the vesicle wall is composed of multiple micron-scale layers of N-rich material. This material exhibited 100-nm-scale texture in the NanoSIMS-HR $^{12}C^{14}N^-$ image that is not visible in the TEM image, which we suspect was caused by extended ion bombardment.

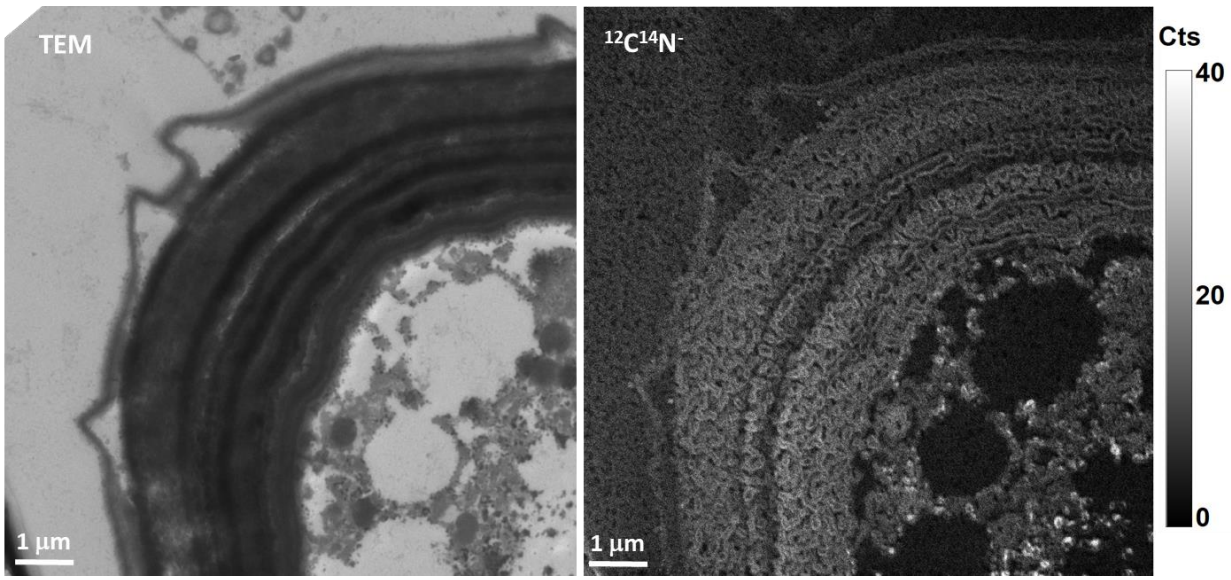


**Figure 3.** Correlated TEM and NanoSIMS-HR $CN^-$ images of an AMF vesicle in a *P. hallii* root. Implantation before data collection ~ $3x10^{15}$ $Cs^+/cm^2$

*Lateral and depth resolution with lower impact energy*

The standard NanoSIMS impact energy of 16 keV is optimized to provide high lateral resolution and high transmission but is expected to result in worse depth resolution than lower impact energies as the primary ions penetrate deeper into the samples. We investigated this trade off with lateral and depth resolution measurements.

Lateral resolution was measured at 16, 8, 4, and 2 keV on the Al-Si sample. As expected, lateral resolution decreased with impact energy (Fig. 4 & S3). The degradation of lateral resolution between 16 keV and 2 keV was on the order of a factor of 5 to 10 depending on beam current.

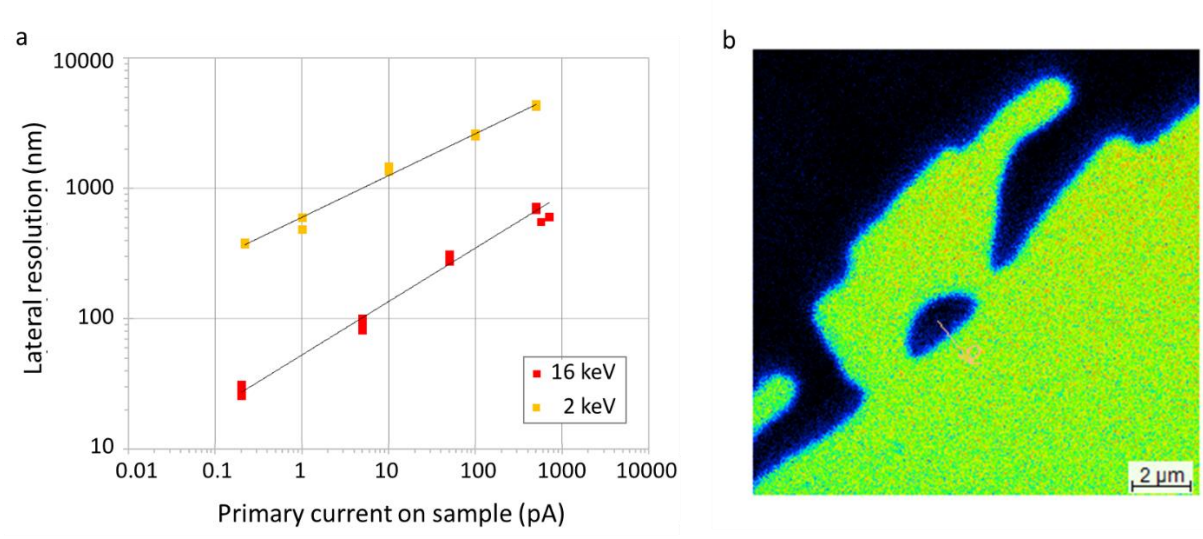


**Figure 4.** (a) Comparison of $Cs^+$ primary current vs. lateral resolution for the NanoSIMS-HR with 16 and 2 keV impact energy. (b) NanoSIMS-HR $Si^-$ ion image of silicon grain in Al-Si sample using $\underline{\leq}$0.2 pA $Cs^+$ at 2 keV. Lateral resolution = 378 nm.

Depth resolution was measured on the trailing edge of P delta layers deposited on a silicon wafer (Fig. 5 and Table 1; see Methods for sample and measurement descriptions). The results are expressed as the depth in which the $^{31}P^-$ count rate declined by a decade (nm/decade). The depth resolutions for the two surface layers are not used because they are too close to the next deeper layer, resulting in $^{31}P^-$ counts from the deeper layer interfering with the measurement. Based on the two deeper layers, the depth resolution is ~22 nm/decade at the 16 keV impact energy, ~15 nm/decade at 8 keV and ~12 nm/decade at 4 keV.

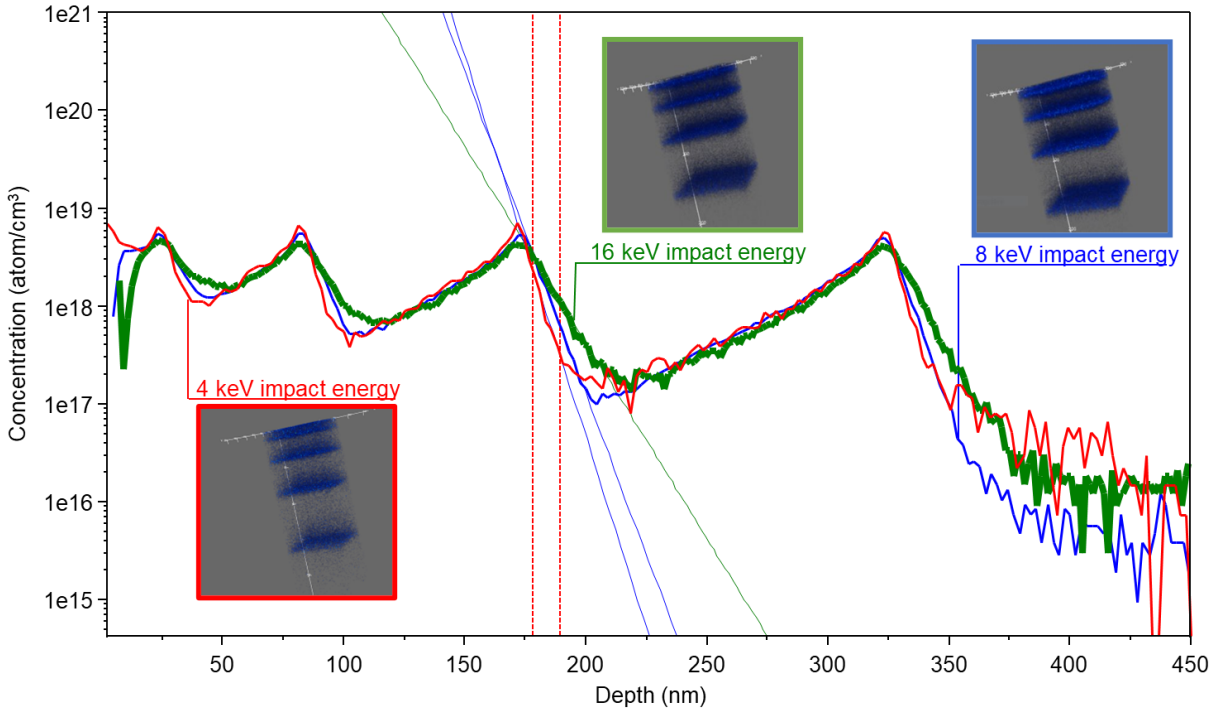


**Figure 5.** P depth profiles in a phosphorus-silicon delta layer sample with 16, 8 and 4 keV $Cs^+$ impact energy. Inset images show 2D projections of the 3D distribution of the $^{31}P^-$ ions detected with depth in the silicon matrix for the three profiles. Note that depth resolution is measured on the trailing edge of the P delta layer because it presents a sharp chemical contrast (see Experimental Section).

**Table 1.** Depth resolution as a function of primary impact energy.

| | **Depth resolution (nm/decade $^{31}P^-$ counts)** | | |
|---|---|---|---|
| **Delta layer** | **16keV** | **8keV** | **4keV** |
| #1 (30nm) | 34 | 20 | 14 |
| #2 (90nm) | 29 | 16 | 13 |
| #3 (180nm) | 22 | 15 | 12 |
| #4 (330nm) | 22 | 14 | 11 |

*Detection limit for P*

A Si wafer implanted with a known dose of P was used to determine the minimum P detection limit and corresponding minimum raster size and optimum ROI for a range of $Cs^+$ primary ion currents (Fig. 6, S4 & S5). The detection limit for P improved from $10^{17}$ atoms per cubic centimeter (at./cm$^3$) for 10 pA $Cs^+$ with a 0.6 x 0.6 µm$^2$ ROI from a 2 x 2 µm$^2$ raster, to $10^{14}$ at./cm$^3$ for 8 nA $Cs^+$ with a 12 x 12 µm$^2$ ROI from a 40 x 40 µm$^2$ raster. We found a consistent relationship between detection limit, minimum raster size and relative ROI size (Fig. 6). The detection limit was lower for higher beam currents because of the larger dynamic range between the peak of the P implant and the tail, but the raster size had to be increased to obtain the minimum detection limit because the primary beam diameter increased with beam current [3].

We found that the minimum raster size was approximately 20 to 30 times the beam diameter, and the optimum ROI was approximately 10% of the raster area (Fig. S5).

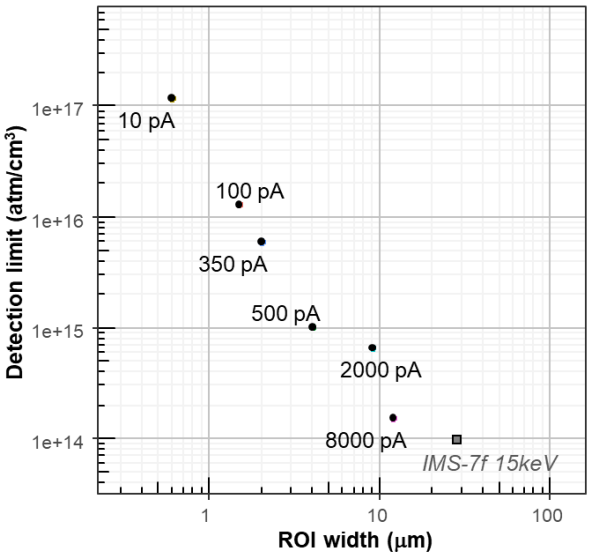


**Figure 6.** P detection limit for 10 to 8000 pA (16 keV) vs. ROI width. These ROIs are ~10% of the total raster size. The $Cs^+$ current in pA is on the sample. IMS-7f data for comparison.

*Stage reproducibility*

The X and Y reproducibility of the sample stage was tested by moving the sample back and forth between the SIMS analysis position and the optical microscope and collecting an ion image eight times (Table 2). Shifts in the imaged feature are measured as pixel shifts and translated to nm based on the number of pixels per nm for the collected images. The observed reproducibility was ≤ 250 nm, which is well within the 500 nm specification.

**Table 2.** Stage movement reproducibility as measured by shift between images with image 1 as the reference.

| Image number | Vertical shift (nm) | Horizontal shift (nm) |
|---|---|---|
| 1 | 0 | 0 |
| 2 | 0 | -94 |
| 3 | 235 | 47 |
| 4 | 282 | 71 |
| 5 | 235 | 212 |
| 6 | 141 | 118 |
| 7 | 424 | -94 |
| 8 | 612 | -118 |
| **1 SD** | **207** | **117** |

*Isotopic ratios*

No significant changes were made to the double focusing mass spectrometer part of the instrument, and therefore no change in isotopic ratio measurement performance was anticipated for the NanoSIMS-HR, and none was found (Table 3; Fig. S6). All measurements were within the precision specified for both instruments, and in this case, all but one had sub-permil precision (1σ). For the Si isotope measurements, high current analyses with Faraday cups achieved ~10x higher precision for the small (microns) and medium (millimeters) movement test, and ~2x higher precision for the large (10s of millimeters) movement test, relative to the lower current analyses with EMs. The O isotope measurements with Faraday cups and the electron flood gun (e-gun) also achieved sub-permil precision.

**Table 3.** Isotopic ratio measurement relative standard deviation (RSD). See Table S1 for test details.

| **Test** | **Specification (50L and HR)** | RSD |
|---|---|---|
| **A:** $^{29}Si/^{28}Si$ and $^{30}Si/^{28}Si$ on silicon wafers using electron multipliers only | **Test A1:** RSD (1σ) ≤ 1.25 ‰<br>10 analyses separated by 20 µm | 0.63 ‰ $^{29}Si/^{28}Si$<br>0.57 ‰ $^{30}Si/^{28}Si$ |
| | **Test A2:** RSD (1σ) ≤ 1.40 ‰<br>10 analyses, deflection mode within 35 x 35 $\mu m^2$ area | 0.73 ‰ $^{29}Si/^{28}Si$<br>0.93 ‰ $^{30}Si/^{28}Si$ |
| | **Test A3:** RSD (1σ) ≤ 1.25 ‰<br>16 analyses, stage moves across 8x8 $mm^2$ area | 0.85 ‰ $^{29}Si/^{28}Si$<br>0.91 ‰ $^{30}Si/^{28}Si$ |
| | **Test A4:** RSD (1σ) ≤ 1.65 ‰<br>12 analyses, 5 different samples | 1.02 ‰ $^{29}Si/^{28}Si$<br>0.80 ‰ $^{30}Si/^{28}Si$ |
| **B:** $^{29}Si/^{28}Si$ and $^{30}Si/^{28}Si$ on silicon wafers using Faraday cups only | **Test B1:** RSD (1σ) ≤ 0.45 ‰<br>10 10x10 $\mu m^2$ analyses separated by 20 µm | 0.13 ‰ $^{29}Si/^{28}Si$<br>0.06 ‰ $^{30}Si/^{28}Si$ |
| | **Test B2:** RSD (1σ) ≤ 0.60 ‰<br>16 10x10 $\mu m^2$ analyses across an 8x8 $mm^2$ | 0.08 ‰ $^{29}Si/^{28}Si$<br>0.08 ‰ $^{30}Si/^{28}Si$ |
| | **Test B3:** RSD (1σ) ≤ 0.80 ‰<br>12 10x10 $\mu m^2$ analyses, 5 different samples | 0.30 ‰ $^{29}Si/^{28}Si$<br>0.56 ‰ $^{30}Si/^{28}Si$ |
| **C:** $^{18}O/^{16}O$ on quartz using Faraday cups only | **Test C1:** RSD (1σ) ≤ 0.80 ‰<br>10 10x10 $\mu m^2$ analyses separated by 20 µm | 0.17 ‰ $^{18}O/^{16}O$ |
| | **Test C2:** RSD (1σ) ≤ 1.00 ‰<br>16 10x10 $\mu m^2$ analyses across an 8x8 $mm^2$ | 0.54 ‰ $^{18}O/^{16}O$ |

**Discussion**

Our tests on the newly redesigned CAMECA NanoSIMS, called the NanoSIMS-HR, demonstrate that features of the new instrument substantially improve imaging, depth profiling, detection limits and automated performance while maintaining secondary ion mass spectrometer performances, such as

mass resolution, transmission, and isotope analyses presented here. The redesigned higher intensity thermal $Cs^+$ ion source is central to the improved performance, but other upgrades such as high-voltage control, an encoded sample stage, a higher resolution optical system, an automated sample exchange system, and new electronics further contribute to improved performance. The ion optics, secondary ion mass spectrometer and multicollection detector system are unchanged.

The redesigned, higher intensity $Cs^+$ ion source is a significant benefit of the NanoSIMS-HR. While the NanoSIMS 50 and 50L instruments had to meet the 50 nm lateral resolution specification, researchers have pushed to improve on this benchmark. Some researchers have reported better than 50 nm lateral resolution for the standard thermal $Cs^+$ ion source on NanoSIMS 50 series [26, 27], but such performance would not be guaranteed by CAMECA. Others have sought to redesign the $Cs^+$ ion source to improve its intensity with some reported success [14, 15], but no product is available yet for testing. Therefore, a reliable and commercially backed instrument that produces a 30 nm lateral resolution $Cs^+$ beam and overall higher $Cs^+$ current density is a significant advance for consumer access.

The ion images of biological samples in this study show the benefit of the improved lateral resolution. The NanoSIMS-HR was able to resolve finer features, such as the holes in the *P. tricornutum* cell wall (Fig. 2) and the structure of the contents of the AMF vesicle (Fig. 3). The relationship between imaging lateral resolution and analytical lateral resolution is somewhat complicated because it includes feature composition, feature spacing, analyte and analyte background [28], but in any case, improved resolution has benefits for navigation and feature identification. It is worth noting that although the highest resolution measurements in this study were made at low MRP to optimize the number of detected ions during a scan to achieve more accurate measurements of the analysis spot size, the same resolution scans could be made with higher MRP. For trace element and isotope analyses, multiple scans are typically made of an analysis area to accumulate statistically meaningful counts of the minor species.

While “ultimate resolution” is the featured specification, the higher current density benefits all analyses by enabling faster analyses, improving low impact energy imaging depth profiling, and lowering detection limits. For example, bacterial analyses with 100 nm lateral resolution can be performed at least 2.5 times faster with the NanoSIMS-HR (5 pA vs. 2 pA for 50L; Fig. 1 & 2). The majority of published papers do not use the ultimate resolution of the NanoSIMS 50 or 50L but rather a lower-resolution, higher-current primary ion beam setting that allows faster analyses, lower detection limits, and generally more straight forward operation. One notable point is that secondary electron imaging, which can be used with the $Cs^+$ ion source for navigation and feature identification, can be very poor at the very low primary current setting (~0.2 pA) necessary to achieve the ultimate resolution.

The ability to vary the NanoSIMS-HR source and sample high voltage from 8 keV down to 1 keV allows the user to trade off lateral resolution for depth resolution. Our results show that at 4 keV impact energy (2 keV on source, -2 keV on the sample), there is an approximately 2-fold improvement in depth resolution with an approximately 5-fold loss in lateral resolution. While the actual lateral resolution is better than it would have been with the previous thermal $Cs^+$ source, the source intensity is still affected by reducing the source high voltage because it extracts the electrons that heat the source, and the ability of the electronics to compensate has limits.

We tested the P detection limit with 10 to 8000 pA $Cs^+$ primary beam current. The improvement in the detection limit with higher beam current reflects the increase in the dynamic range between the

implanted P and the background [3]. The relationship between beam current and detection limit in the P analyses in this study reflects an optimal relationship between the primary current resolution, the sputtered area and the target area for data extraction (Fig. 6). We found that the optimum relationship between primary beam diameter and raster size was a factor of 20 to 30. Smaller rasters result in significant contribution of $P^-$ counts from the periphery of the analysis crater to the central ROI. We also found that the optimal ROI size is ~10% of the raster size; smaller ROIs result in a reduced dynamic range and limitation on the number of atoms in the analyzed area (Fig. S5). We do not have comparable 50L data, but we would expect the ROI for any given detection limit to be larger because of the lower beam intensity. Based on previous work, the minimum size that a feature of interest could be is the size of the ROI plus two beam widths [3].

Higher primary beam current density also lowers background for analyses such as H and O, where the background count rate is proportional to the rate at which these species in the analysis chamber vacuum interact with the sample surface [29]. Higher spatial resolution also increases sensitivity to the composition of the target feature by sampling the feature and not the adjacent material.

The improved stage control can further speed up automated analyses by allowing the primary beam raster to be more tightly framed on a series of preselected targets, such as cells or particles. The analysis area has to be scaled based on the stage precision to ensure that selected targets are hit. The proportional increase in area directly translates to analysis time to collect sufficient ions from the target. The greatest improvement is for small targets (e.g., 1 μm ϕ), where the increase in analysis speed would be between 30 and 100 times, depending on whether one allows for 5- or 10-micron stage reproducibility with a NanoSIMS 50L (analysis time is proportional to the square of the target size + 2x stage reproducibility; Fig. S7). For larger targets, the increase in analysis speed reduces geometrically down to 2 to 3 times for 30-micron diameter targets, which is still a significant time savings.

**Conclusion**

The NanoSIMS-HR provides improved spatial resolution, detection limits, and throughput compared to its predecessors, the NanoSIMS 50 and 50L. The improved thermal $Cs^+$ ion source is central to the improved performance of the NanoSIMS-HR, while features like HV control, improved navigation, and a precision stage also provide significant benefits.

**Supporting Information**

Table S1. CAMECA NanoSIMS-HR and 50L tests and specifications for isotope measurements.
Table S2. CAMECA NanoSIMS-HR lateral resolution specifications.
Fig. S1. Examples of lateral resolution measurements at 16 keV impact energy.
Fig. S2. Correlated TEM and NanoSIMS-HR CN- images of an AMF vesicle in a P. hallii root at 16 keV impact energy.
Fig. S3. Resolution at low impact energy.
Fig. S4. Comparison of P depth profiles and detection limits for 100 versus 8000 pA Cs+.
Fig. S5. P detection limit versus ROI size for individual analyses.
Fig. S6. Isotope measurement plots for the nine specification tests.
Fig. S7. Relative analysis time factor as a function of target size for the NanoSIMS 50L vs. NanoSIMS-HR.

**Acknowledgements**

We thank the reviewers for detailed reviews that greatly improved this manuscript. Primary funding for this research was provided by U.S. Department of Energy (DOE) Office of Biological and Environmental Research (BER) award SCW1039. Support to JPR was provided by DOE BER award SCW1632, and support to RH was provided by the Foundation for Food & Agriculture Research under award number 23-000585. Instrumentation funding was provided by DOE BER and Lawrence Livermore National Laboratory (LLNL). Research at LLNL was performed under the auspices of DOE under Contract DE-AC52-07NA27344.

[#]M.M: Oak Ridge Institute for Science and Education, P.O. Box 117, Oak Ridge, TN 37831, USA.

## References

1. Castaing, R.; Slodzian, G. Microanalyse par emission ionique secondaire. *Journal of Microscopy* **1962**, *1*, 31-38.
2. Castaing, R.; Slodzian, G. Microanalysis using secondary ion emission By Raimond Castaing and Georges Slodzian. *Journal of Mass Spectrometry* **2021**, *56* (12), e4575. DOI: https://doi.org/10.1002/jms.4575.
3. Wilson, R. G.; Stevie, F. A.; Magee, C. W. *Secondary Ion Mass Spectrometry: A Practical Handbook for Depth Profiling and Bulk Impurity Analysis*; Wiley, 1989.
4. Slodzian, G.; Daigne, B.; Girard, F.; Boust, F.; Hillion, F. Scanning secondary ion analytical microscopy with parallel detection. *Biol Cell* **1992**, *74*, 43 - 50.
5. Slodzian, G.; Daigne, B.; Girard, F.; Boust, F.; Hillion, F. A high-resolution scanning ion microscope with parallel detection of secondary ions. In *Proceedings of the 8th International Conference for Secondary Ion Mass Spectrometry 1991, SIMS VIII*, Benninghoven, A., Janssen, K. T. F., Tumpner, J., Werner, H. W. Eds.; John Wiley & Sons, 1992; pp 169-178.
6. Hillion, F.; Daigne, B.; Girard, F.; Slodzian, G. A new high performance instrument: the CAMECA NanoSIMS 50. In *Secondary Ion Mass Spectrometry: SIMS IX*, Benninghoven, A., Nihei, Y., Shimizu, R., Werner, H. W. Eds.; John Wiley & Sons, 1993; pp 254-257.
7. Stadermann, F. J.; Walker, R. M.; Zinner, E. Nanosims: The next generation ion probe for the microanalysis of extraterrestrial material. *Meteoritics & Planetary Science* **1999**, *34*, A111-A112.
8. Daulton, T. L.; Bernatowicz, T. J.; Lewis, R. S.; Messenger, S.; Stadermann, F. J.; Amari, S. Polytype Distribution in Circumstellar Silicon Carbide. *Science* **2002**, *296* (5574), 1852-1855. DOI: doi:10.1126/science.1071136.
9. Messenger, S.; Keller, L. P.; Stadermann, F. J.; Walker, R. M.; Zinner, E. Samples of stars beyond the solar system: silicate grains in interplanetary dust. *Science* **2003**, *300*, 105 - 108.
10. Zinner, E.; Amari, S.; Guinness, R.; Nguyen, A.; Stadermann, F. J.; Walker, R. M.; Lewis, R. S. Presolar spinel grains from the Murray and Murchison carbonaceous chondrites. *Geochimica Et Cosmochimica Acta* **2003**, *67* (24), 5083-5095.
11. Besmehn, A.; Hoppe, P. A NanoSIMS study of Si- and Ca-Ti-isotopic compositions of presolar silicon carbide grains from supernovae. *Geochimica Et Cosmochimica Acta* **2003**, *67* (24), 4693-4703.
12. Hoppe, P. NanoSIMS perspectives for nuclear astrophysics. *New Astronomy Reviews* **2002**, *46* (8-10), 589-595.
13. Smith, N.; Tesch, P.; Martin, N.; Kinion, D. A high brightness source for nano-probe secondary ion mass spectrometry. *Applied surface science* **2008**, *255* (4), 1606-1609.
14. Williams, P.; Williams, K. A.; Bose, M.; Prince, J. Cesium primary ion source for secondary ion mass spectrometer. U.S.A. 2020.

15. Peter Williams, M. B., Lynda Williams, Richard Hervig. Improved cesium and oxygen primary ion source designs for SIMS. In *The 22nd International Conference on Secondary Ion Mass Spectrometry*, Kyoto, Japan, 2019.
16. Williams, P. Duoplasmatron ion source with a partially ferromagnetic anode U.S.A. 2021.
17. Ghosal, S.; Fallon, S. J.; Leighton, T.; Wheeler, K. E.; Hutcheon, I. D.; Weber, P. K. Imaging and 3D elemental characterization of intact bacterial spores with high-resolution secondary ion mass spectrometry (NanoSIMS) depth profile analysis. *Analytical Chemistry* **2008**, *80* (15), 5986–5992.
18. Mayali, X.; Samo, T. J.; Kimbrel, J. A.; Morris, M. M.; Rolison, K.; Swink, C.; Ramon, C.; Kim, Y.-M.; Munoz-Munoz, N.; Nicora, C.; et al. Single-cell isotope tracing reveals functional guilds of bacteria associated with the diatom Phaeodactylum tricornutum. *Nature Communications* **2023**, *14* (1), 5642. DOI: 10.1038/s41467-023-41179-9.
19. Harding, K. J.; Turk-Kubo, K. A.; Mak, E. W. K.; Weber, P. K.; Mayali, X.; Zehr, J. P. Cell-specific measurements show nitrogen fixation by particle-attached putative non-cyanobacterial diazotrophs in the North Pacific Subtropical Gyre. *Nature Communications* **2022**, *13*.
20. Hoppe, P.; Cohen, S.; Meibom, A. NanoSIMS: Technical Aspects and Applications in Cosmochemistry and Biological Geochemistry. *Geostandards and Geoanalytical Research* **2013**, *37* (2), 111-154. DOI: 10.1111/j.1751-908X.2013.00239.x.
21. Malherbe, J.; Penen, F.; Isaure, M.-P.; Frank, J.; Hause, G.; Dobritzsch, D.; Gontier, E.; Horréard, F. o.; Hillion, F. o.; Schaumlöffel, D. A new radio frequency plasma oxygen primary ion source on nano secondary ion mass spectrometry for improved lateral resolution and detection of electropositive elements at single cell level. *Analytical chemistry* **2016**, *88* (14), 7130-7136.
22. P. Thévenaz, U. E. R., M. Unser. A Pyramid Approach to Subpixel Registration Based on Intensity. *IEEE Transactions on Image Processing* **1998**, *7* (1), 27-41.
23. Pett-Ridge, J.; Weber, P. K. NanoSIP: NanoSIMS applications for microbial biology. In *2nd edition of Microbial Systems Biology: Methods and Protocols. Methods in Molecular Biology, Springer Protocols*, A. Navid Ed.; Humana Press, New York, 2022.
24. Ito, M.; Nagasawa, H.; Yurimoto, H. Oxygen isotopic SIMS analysis in Allende CAI: details of the very early thermal history of the solar system1 1Associate editor: U. Ott. *Geochimica et Cosmochimica Acta* **2004**, *68* (13), 2905-2923. DOI: https://doi.org/10.1016/j.gca.2004.02.001.
25. Ito, M.; Messenger, S. R. Isotopic imaging of refractory inclusions in meteorites with the NanoSIMS 50L. *Applied Surface Science* **2008**, *255*, 1446-1450.
26. Hoppe, P.; Ott, U.; Lugmair, G. W. NanoSIMS, the new tool of choice: 26Al, 44Ti, 49V, 53Mn, 60Fe, and more. *New Astronomy Reviews* **2004**, *48* (1), 171-176. DOI: https://doi.org/10.1016/j.newar.2003.11.025.
27. Lechene, C.; Hillion, F.; McMahon, G.; Benson, D.; Kleinfeld, A.; Kampf, J. P.; Distel, D.; Luyten, Y.; Bonventre, J.; Hentschel, D.; et al. High-resolution quantitative imaging of mammalian and bacterial cells using stable isotope mass spectrometry. *Journal of Biology* **2006**, *5* (6), 20.
28. Chabala, J. M.; Levi-Setti, R.; Wang, Y. L. Practical resolution limits of imaging microanalysis with a scanning ion microprobe. *Applied Surface Science* **1988**, *32*, 10-32.
29. Kudriavtsev, Y.; Villegas, A.; Godines, A.; Asomoza, R. SIMS analysis of residual gas elements with a Cameca IMS-6f ion microprobe. *Applied Surface Science* **2006**, *252* (10), 3406-3412. DOI: https://doi.org/10.1016/j.apsusc.2005.05.064.